

Role of crystal and magnetic structures in the magnetoelectric coupling in $\text{CaMn}_7\text{O}_{12}$

Jhuma Sannigrahi^{1,2}, Md Salman Khan³, Mohamad Numan⁴, Manjil Das⁴, Anupam Banerjee⁴, Manh Duc Le²,
Giannantonio Cibin⁵, Devashibhai Adroja^{2,6}, and Subham Majumdar⁴

¹*School of Physical Sciences, Indian Institute of Technology Goa, Farmagudi, Goa 403401, India*

²*ISIS Neutron and Muon Source, Science and Technology Facilities Council, Rutherford Appleton Laboratory,
Didcot OX11 0QX, United Kingdom*

³*Department of Energy Science, Sungkyunkwan University, Suwon 16419, Republic of Korea*

⁴*School of Physical Sciences, Indian Association for the Cultivation of Science, 2A & B Raja S. C. Mullick Road,
Jadavpur, Kolkata 700 032, India*

⁵*Diamond Light Source Ltd., Diamond House, Harwell Science and Innovation Campus, Didcot, Oxfordshire OX11 0DE, United Kingdom*

⁶*Highly Correlated Matter Research Group, Physics Department, University of Johannesburg, P.O. Box 524,
Auckland Park 2006, South Africa*



(Received 14 December 2023; accepted 22 January 2024; published 13 February 2024)

We investigate the magnetoelectric coupling in $\text{CaMn}_7\text{O}_{12}$ (CMO) through a comprehensive spectroscopic analysis combining inelastic neutron scattering (INS), x-ray absorption spectroscopy (XAS), and synchrotron-based powder x-ray diffraction (PXRD). CMO's intricate interplay between magnetism and ferroelectricity is dissected to uncover its underlying mechanisms. XAS reveals a mixed valency of Mn ions in CMO, reflecting the presence of Mn^{3+} and Mn^{4+} ions, which contributes to its magnetoelectric properties. The double structure in Mn-K near-edge absorption spectra reinforces multiple Mn sites as well as the mixed valency of the compound. Synchrotron-based PXRD experiments conducted over a range of temperatures unveil structural distortions near the magnetic transition temperatures of CMO. These distortions coincide with anomalies in lattice parameters and bond lengths, shedding light on the link between structural modulations and magnetoelectric behavior. Furthermore, INS measurements identify specific energy bands (E_1 , E_2 , and E_3) associated with distinct exchange interactions between Mn ions. This work advances our understanding of magnetoelectric coupling mechanisms and showcases the potential of multifunctional materials for applications in spintronics and related fields.

DOI: [10.1103/PhysRevB.109.054417](https://doi.org/10.1103/PhysRevB.109.054417)

I. INTRODUCTION

Magnetic multiferroics, in which ferroelectricity is induced by magnetic ordering, have had significant impact in condensed matter physics over the last few decades [1–5]. The magnetoelectric effect was discovered by Curie at the end of the 19th century [6]. However, it started to attract the scientific communities almost a century later when multiferroic materials with a magnetoelectric effect showed potential applications for multifunctional devices. The interplay between the magnetic and electric order parameters is fascinating from a technological point of view. Many multiferroics have too small value of magnetoelectric coupling to be viable for mass-scale applications. A few decades ago, some rare-earth manganites, RMnO_3 and RMn_2O_5 (R = rare-earth element), started to show stronger coupling between antiferromagnetism and ferroelectricity and, as a result, provided larger values of ferroelectric polarization [1,4]. For example, for electrical polarization (P) in the well-known magnetic

multiferroics TbMnO_3 [1], DyMnO_3 [7], and TbMn_2O_5 [4], the spontaneous polarizations are found to be 0.08, 0.2, and $0.04 \mu\text{Ccm}^{-2}$, respectively.

In the recent past, a relatively large, magnetically induced spontaneous polarization was observed in a few multiferroics, such as $\text{CaMn}_7\text{O}_{12}$ [8–11], epitaxial thin film of YMnO_3 [12], $\text{Cu}_2\text{V}_2\text{O}_7$ [13], etc. Among them, $\text{CaMn}_7\text{O}_{12}$ has acquired the largest measured ferroelectric polarization value ($\sim 3000 \mu\text{Ccm}^{-2}$) below ~ 90 K in the single-crystalline sample so far.

$\text{CaMn}_7\text{O}_{12}$ (CMO) adopts a rhombohedral phase characterized by the space group $R\bar{3}$ at temperatures below about 440 K. This compound is classified within the quadruple ($\text{AA}'_3\text{B}_4\text{O}_{12}$) family of manganites exhibiting a perovskite-derived crystal structure. CMO is a mixed-valent manganese compound, comprising both Mn^{3+} and Mn^{4+} ions, forming a charge-ordered state at temperatures below about $T_{\text{CO}} = 240$ K. There exist three inequivalent Mn sites, labeled Mn1, Mn2, and Mn3 [10], occupying Wyckoff positions $9e$, $9d$, and $3b$, respectively, as illustrated in Fig. 1. CMO can be represented as $[\text{CaMnI}_3^{3+}]_A[\text{Mn}_2^{3+}\text{Mn}^{3+}]_B\text{O}_{12}$, where perovskite sites A are occupied by three Mn^{3+} ions, while sites B are filled by the remaining four Mn ions, maintaining a ratio of Mn^{3+} to Mn^{4+} of 6:1. Below T_{CO} , the Mn^{3+} , Mn^{2+} , and Mn^{3+} ions arrange themselves into distinct structural units: MnIO_4 square planes, the axially compressed Mn_2O_6

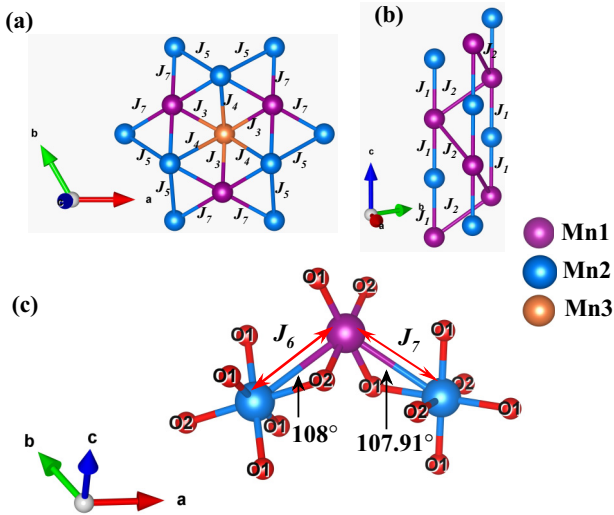


FIG. 1. (a), (b) The seven exchange couplings between different Mn atoms. For clarity, we showed only Mn atoms with a parallel view. (c) Difference in exchange interaction pathways between the two Mn1-Mn2 couplings with equal bond length.

octahedra, and the Mn_3O_6 octahedra, respectively. In the charge-ordered state, the material shows structural modulation and, at 60 K, the structural modulation vector is found to be $\mathbf{k}_s = (0, 0, 0.9213)$ [14]. In particular, the magnitude of \mathbf{k}_s exhibits a weak temperature (T) dependence, initially increasing with decreasing temperature down to approximately 100 K, and eventually showing a decreasing trend. In contrast, Johnson *et al.* [15] found that the magnitude of \mathbf{k}_s is almost T independent down to 48 K, below which it shows a decrease in its value. The Mn-O distance also shows a modulation as we move in the coordinate space [14].

Below the Néel temperature $T_{N1} = 90$ K, CMO displays an incommensurate magnetic structure (AFMI state) characterized by the propagation vector $\mathbf{k}_1 = (0, 1, 0.963)$. At lower temperatures, below about $T_{N2} = 48$ K, two modulations with propagation vectors $\mathbf{k}_2 = (0, 1, 0.880)$ and $\mathbf{k}_3 = (0, 1, 1.042)$ coexist (AFMII state). [10] However, in a recent work, Johnson *et al.* [15] claimed that there can be an infinite number of magnetic propagation vectors below T_{N2} , of which they can distinctly detect four of them in their neutron diffraction data. Lu *et al.* [8] explained the observed magnetic structure on the basis of a spin dimer model and evaluated the magnetic exchange interaction terms J_i ($i = 1, 2, \dots, 7$) (see Fig. 1) using the density functional theory (DFT)+ U formalism. The exchange terms have mixed signs (positive and negative), indicating the presence of both ferromagnetic and antiferromagnetic couplings between Mn ions.

The exchange interaction J_1 between adjacent Mn^{13+} and Mn^{23+} ions parallel to the crystallographic c direction is found to be strongly ferromagnetic (FM) ($J_1 = -5.57$ meV), while J_2 between two Mn^{13+} spins along two adjacent chains running parallel to the c axis is strongly antiferromagnetic (AFM) ($J_2 = 6.37$ meV) (see Fig. 1). $J_3 (= -3.916$ meV) is the FM exchange interaction between Mn^{13+} and Mn^{34+} . The interaction between Mn^{23+} and Mn^{34+} is also FM and denoted by $J_4 (= -2.961$ meV). The interchain interaction

between two Mn^{23+} ions on two adjacent chains parallel to the c direction is FM ($J_5 = -2.534$ meV). J_6 and J_7 are interactions between Mn^{13+} and Mn^{23+} from two adjacent chains on both sides. If we consider Mn^{13+} from the middle chain, then J_6 is FM ($= -2.290$ meV) and J_7 is AFM ($= 2.412$ meV), although the bond lengths are the same.

The electric polarization observed below T_{N1} is remarkably high, and the direction of \mathbf{P} lies perpendicular to the plane of rotation of Mn spins in the helical magnetic structure [10]. This rules out a simple spin current model for the observed multiferroicity. In the last decade, there have been numerous experimental and theoretical works on the magnetic and electrical polarization of the compound [8–10, 15–20]. While Johnson *et al.* [10] proposed a ferroaxial model for polarization, Lu *et al.* [8] conjectured that the large \mathbf{P} would originate from the combined effect of the Dzyaloshinskii-Moriya (DM) interaction and the exchange striction. In the latter model, the magnitude of \mathbf{P} is determined by the exchange striction, and the DM interaction determines its direction. On the other hand, Dai *et al.* [18] considered that the actual crystal structure of CMO has a noncentrosymmetric ground state with spontaneous polarization. Furthermore, the p - d metal-ligand hybridization in tandem with exchange striction was proposed for the large \mathbf{P} [19, 20]. Evidently, the mechanism behind the multiferroicity in the compound remains elusive.

The crystal and magnetic structures of CMO are notably intricate, featuring an incommensurate modulation. The interplay between these structures appears to play a pivotal role in the observed strong magnetoelectric coupling and giant spontaneous polarization in CMO. To delve deeper into this phenomenon, we have employed macroscopic and microscopic temperature-dependent techniques, including powder x-ray diffraction (PXRD), x-ray absorption spectroscopy (XAS), and inelastic neutron scattering (INS).

II. EXPERIMENTAL DETAILS

A polycrystalline sample of CMO was synthesized using the sol-gel technique described in our previous report [11]. The sample was investigated through high-resolution T -dependent x-ray diffraction using the synchrotron facility (wavelength 0.855 Å) at the Indian beam line at the Photon Factory, National Laboratory for High Energy Physics (KEK), Japan, between 20 and 300 K. The PXRD data have been refined using the JANA2020 software package [21, 22]. Pellets of CMO powder sample diluted with cellulose were prepared with an optimized density for the Mn K -edge x-ray absorption spectroscopy at the B18 beam line at the Diamond Light Source (Oxfordshire, UK). The XAS measurements were performed in the transmission mode at different temperatures using a He-4 closed-cycle refrigerator. The collected XAS data were processed and analyzed using the freely available DEMETER package [23, 24].

The INS measurements were performed on the time-of-flight spectrometer MERLIN at the ISIS Neutron and Muon Facility, Rutherford Appleton Laboratory, United Kingdom [25, 26]. An approximately 9 g powder sample of CMO was placed in an envelope of thin Al foil with 40 mm height and 140 mm length. The envelope was rolled into a cylindrical form and inserted inside an aluminium can of 40 mm

diameter with a 0.1-mm-thick wall. The aluminium can was then inserted inside a He-4 closed-cycle refrigerator for low- T measurements. The straight Gd slit package was used in the Fermi chopper, which was phased at a rotation speed of 350 Hz to allow the recording of spectra with incident energies of 100, 38, 20, and 12.30 meV, simultaneously, via the repetition-rate multiplication method [27,28]. The data were collected at several temperatures between 5 and 300 K. To obtain the scattering intensity in the units of cross section, $\text{mb sr}^{-1} \text{meV}^{-1} \text{f.u.}^{-1}$, vanadium spectra were recorded with identical conditions. The data have been reduced using the MANTID PLOT software [29]. The spin-wave simulations have been carried out using the SpinW package [30].

III. RESULTS AND DISCUSSION

A. Powder x-ray diffraction

The refined PXRD patterns corresponding to temperatures of 300, 150, and 20 K are depicted in Figs. 8(a)–8(c), respectively. Clearly identifiable satellite peaks are observed below 250 K, which exhibit a significantly broader full width at half maximum (FWHM) compared to the primary reflections. Consequently, distinct FWHM values were used for the refinement of fundamental and satellite reflections in the JANA2020 program. The incommensurate structural modulation observed in our study is aptly described using the space group $R\bar{3}(00\gamma)0$ and the propagation vector $(0,0,q)$, where $q = 0.92813(4)$ at 10 K. Our PXRD data prominently identify 78 satellite peaks, mirroring findings previously reported by Sławiński *et al.* [14]. These observed satellite intensities can be quantitatively elucidated by assuming positional modulation of ions within the lattice. Optimal fitting is achieved by considering the positional modulations in the coordinates (x, y, z) pertaining to Mn1, Mn2, O1, and O2, and the modulation of the z coordinate for Mn3 and Ca. These modulation amplitudes decrease as T increases, ultimately disappearing above 250 K.

Figures 2(a) and 2(b) show the T variation of lattice parameters a and c of the envelope structure. We observe clear peaks at around 90 K in both a and c . Below 45 K, both the parameters increase with a lowering of T . We also looked at the Mn-O bond lengths for different sites of Mn and O. The Mn1 atom, sitting at the $9e$ site, can have two different bonds with O1 and O2. Figure 2(c) shows the variation of Mn1-O1 and Mn1-O2 bond lengths with T . Clearly, their variations with T are opposite and the curves look like a mirror image of one another. Both the bond lengths show anomaly at $T_{N1} = 90$ and $T_{N2} = 45$ K. Below T_{N1} , Mn1-O1 increases with a lowering of T , while Mn1-O2 shows decreasing trends. It is to be noted that the variation of the bond-length Mn1-O1 shows a larger variation with T than Mn1-O2. The elongation and the contraction of the bond lengths are depicted in Fig. 2(d). Mn2-O1 can have two different bond lengths, namely, nearest neighbor (NN) and next-nearest neighbor (NNN). Both of them show anomalies at T_{N1} and T_{N2} , and their variations are opposite to each other [see Fig. 2(d) for a schematic representation]. Interestingly, Mn3-O2 shows anomaly only at T_{N2} , which is characterized by a sharp decrease.

B. XANES

From the previous theoretical works [8,17,20], it is evident that the mixed valency of Mn and their crystallographic environments play an important role in the observed polarization. The coordinations of O in three Mn ions are different, leading to dissimilar splitting of the electronic energy levels. For a better understanding of the charge state of Mn as well as their energy configurations, we primarily focused on the x-ray absorption near-edge structure (XANES), which is rather intriguing in the case of this mixed-valent Mn compound having multiple Mn-O coordination.

Figure 3(a) shows the Mn- K near-edge absorption spectra of CMO recorded at 120 K. For comparison, we have also added the XANES spectra of Mn_2O_3 and MnO_2 , where Mn ions are in the $3+$ and $4+$ states, respectively. The rising line of CMO lies slightly above in energy than Mn_2O_3 (Mn^{3+}); nevertheless, it is well below the rising line of MnO_2 (Mn^{4+}). This indicates that Mn in CMO is mostly trivalent along with the presence of minority Mn^{4+} ions. This supports the previous reports of mixed valency of Mn in CMO with the ionic ratio $\text{Mn}^{3+}:\text{Mn}^{4+} = 6:1$. The XANES spectra of CMO were recorded between 120 and 10 K and we do not observe any change in the position of the rising line with T . This indicates that there is no change in the charge state of Mn throughout the T range of measurement.

Below the rising line, a weak humplike feature is visible between 6536 to 6545 eV, which can be assigned to the pre-edge of the Mn- K line [see Fig. 3(b)]. The pre-edge is found to have multiple structures. The pre-edge occurs due to the quadrupole-allowed transition of electrons from the $1s$ to $3d$ level in a transition metal [31] and, consequently, the pre-edge intensity is very low. However, pre-edge can be stronger in the presence of $3d-4p$ (metal to metal) or $3d-2p$ (metal to ligand) hybridization. We have fitted the background of the pre-edge with an arc tangent function [green line in Fig. 3(b)]. Considering two distinct peaks, we have initially tried to fit the pre-edge using two Lorentzian as well as using two pseudo-Voigt functions. However, we failed to get a good fit using two peak functions. The best fit is obtained when we use three pseudo-Voigt functions (peaks P_1 , P_2 , and P_3), as shown in Fig. 3(b).

In the case of LaMnO_3 with Mn^{3+} in the octahedral coordination, two pre-edge peaks are observed around $A_1 = 6539$ and $A_2 = 6541$ eV [31,32]. On the other hand, CaMnO_3 with almost undistorted octahedra and having Mn in the $4+$ state shows a pre-edge peak around $A_3 = 6543$ eV, in addition to A_1 and A_2 peaks. For CMO, we can corroborate the pre-edge peaks P_1 and P_2 to the reported A_1 and A_2 peaks, respectively, which is present in both LaMnO_3 and CaMnO_3 . Similarly, P_3 can be compared to A_3 of CaMnO_3 considering the fact that CMO also contains Mn^{4+} ions. The total area under the three pre-edge peaks P_1 , P_2 , and P_3 in CMO shows notable anomalies with T [see the inset of Fig. 3(b)]. The area shows a sharp drop around T_{N1} and a rise at T_{N2} . The observed changes in the area are within the error limit of our experimental data.

As evident from our analysis of the PXRD data, the Mn1-O1 and Mn1-O2 bond lengths (see Fig. 2) decrease and increase below T_{N1} , respectively. This makes the MnO_4 square planes more symmetric. Similarly, the distortion in MnO_6 octahedra decreases due to the increase and decrease

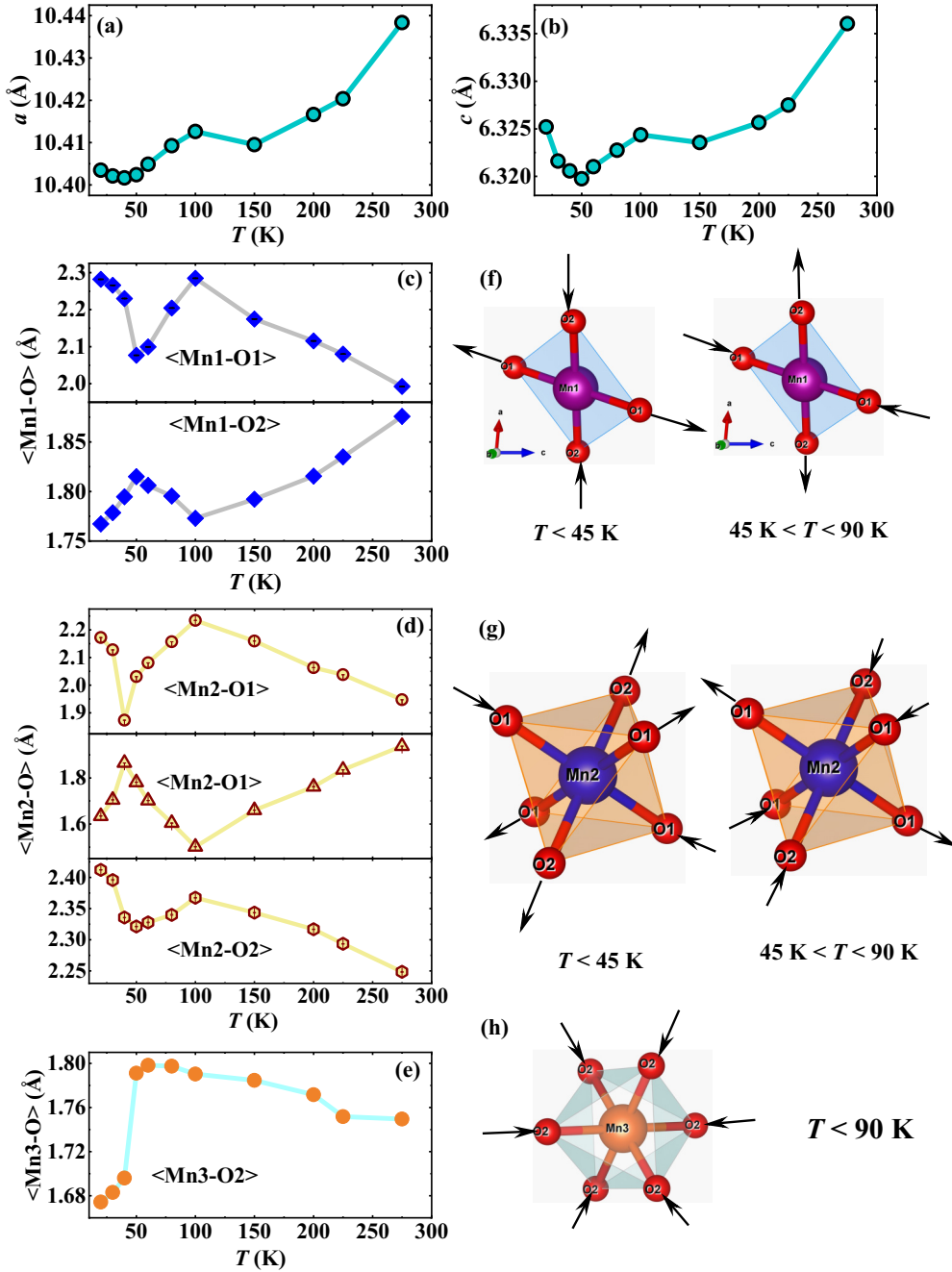


FIG. 2. (a), (b) The variation in lattice parameters as a function of temperature. (c)–(e) The temperature variation of the bond lengths Mn1-O, Mn2-O, and Mn3-O, respectively. (f)–(h) The perspective view of the distortion of the Mn1-O octahedral, Mn2-O square planar, and Mn3-O octahedral structures, respectively, with temperature.

of Mn2-O1 and Mn2-O2 bond lengths, respectively. Such an increase in symmetry may be attributed to the decrease in the pre-edge intensity just below T_{N1} . On the other hand, Mn-O coordination turns less symmetric below T_{N2} , leading to an increase in the pre-edge intensity [31,33,34].

C. Inelastic neutron scattering

1. Spin-wave excitations

Figures 4(a)–4(i) show the two-dimensional (2D) color plots of the inelastic neutron scattering data at different

temperatures with incident energies $E_i = 12.3$, 20, and 38 meV. As these measurements were performed on polycrystalline samples, the magnetic scattering cross section is the powder average of the spin-spin correlation function and does not carry the information regarding the directional property of the momentum transfer, \mathbf{Q} . Nevertheless, it contains the necessary information, which can be readily compared to the theoretical models to ascertain the approximate spin-spin exchange parameters. For CMO, all the observed magnetic intensities are found to be situated below ≈ 30 meV. There are three bands of magnetic scatterings, namely, (a) 2–8 meV,

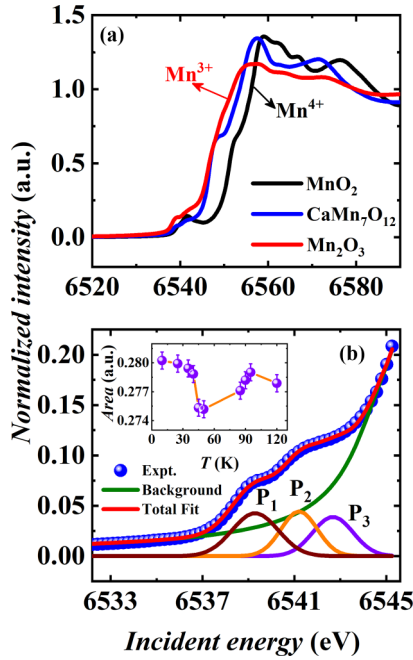


FIG. 3. (a) Mn K -edge XANES data recorded at 120 K along with reference spectra for MnO_2 and Mn_2O_3 . (b) Pre-edge fitting with arc tangent background along with three pseudo-Voigt peak functions. The inset shows the total area of the pre-edge as a function of temperature.

(b) 8.5–15 meV, and (c) 15.5–28 meV. The magnetic nature of these scatterings is evident from the decreasing intensity with increasing $|\mathbf{Q}|$. The bands are detectable up to $\approx 4 \text{ \AA}^{-1}$.

The scattering band over ≈ 2 -8 meV appears to be strongly affected by increasing T . The intensity of this low-energy band weakens quickly above T_{N2} . This implies that this low-energy band is associated with the AFMII long-range ordered state of CMO. The scattering band between 8.5 and 15 meV broadens above T_{N2} [see Figs. 4(d)–4(f)]. On the contrary, the intensity of the scattering band between 15.5 and 28 meV persists up to T_{N1} , indicating its association with the AFMI magnetic state.

The T evolution of the magnetic scattering intensity is better apprehended from the E versus intensity plots summed over the low- Q range, as shown in Fig. 5. At 5 K, for $E_i = 38$ meV, there are three distinct inelastic peaks E_1 , E_2 , and E_3 , which correspond, respectively, to the intensity bands (a) 2–8 meV, (b) 8.5–15 meV, and (c) 15.5–28 meV in our 2D color plots. At 50 K, the low-energy excitations, namely, E_1 and E_2 , vanish, while the high-energy excitation E_3 remains unaltered. It clearly indicates that E_3 is connected to the magnetic ordering at $T_{N1} = 90$ K, while E_1 and E_2 are due to the low- T magnetic order occurring at $T_{N2} = 48$ K. The previous INS work by Kadlec *et al.* [35] observed magnetic scattering at 3.5, 6, and 10 meV energies below about 50 K, which closely match our observed band of excitation energies around E_1 and E_2 . It is evident from both the 2D color plot and the cuts (Figs. 4 and 5, respectively) that the excitation peaks have significant bandwidth with smaller energy gaps. Interestingly, the lowest-energy band around E_1 is dispersive in nature. We do not observe any clear signature of the energy gap between

TABLE I. Magnetic exchange parameters (J_1 , J_2 , J_3 , J_4 , J_5 , J_6 , and J_7) as obtained from DFT calculations (GGA and GGA+ U) and simulated and/or experimental data of the present work.

Model	J_1	J_2	J_3	J_4	J_5	J_6	J_7
	(meV)						
DFT	−5.565	6.368	−3.916	−3.916	−2.534	−2.290	2.412
Simul./Expt.	−5.565	6.068	−2.737	−2.222	−1.711	−2.290	2.412

the ground state and the lowest edge of the excitation spectra within the resolution of the MERLIN instrument.

2. SpinW simulation

In order to model the experimentally observed magnetic excitation, we have calculated spin-wave dispersion using the SpinW software package. Due to three magnetic sites and incommensurately modulated magnetic structure, several exchange interaction pathways between the Mn ions need to be considered. We have considered seven exchange interactions between the different Mn sites following the DFT result by Lu *et al.* [8]. We have constructed the following magnetic Hamiltonian with seven different exchange couplings, DM interactions, and single-ion anisotropy:

$$\mathcal{H} = \sum_{ij} J_{ij} (\vec{S}_i \cdot \vec{S}_j) + \sum_{ij} \vec{D}_{ij} \cdot (\vec{S}_i \times \vec{S}_j) + \sum_i A_\zeta (S_i^\zeta)^2. \quad (1)$$

Here, the first term represents the symmetric Heisenberg interaction, where J_{ij} are the different exchange interactions as discussed before. The second antisymmetric part is related to the DM interaction. The last term is due to the single-ion anisotropy parameter A , which originates from the crystal field of the surrounding oxygen ions in the Mn1O_4 square planar and Mn2O_6 octahedral environments. We did not consider any anisotropy for Mn3 because of the symmetric oxygen environment. We used the values for DM interaction and single-ion anisotropy terms as provided by Lu *et al.* [8]. For the sake of simplicity in the SpinW simulation, we have used only the magnetic propagation vector $\mathbf{k}_1 = (0, 1, 0.963)$ at all temperatures, although there are reports of more than one magnetic propagation vector at low temperatures. We started with the J values provided by Lu *et al.* [8] and, subsequently, they are tuned to reproduce the experimentally obtained INS intensity (see Table I). We have properly combined the energy resolution function of the MERLIN spectrometer ($E_i = 38$ and 12.3 meV) in the SpinW simulation.

Figures 6(a) and 6(b) show the phonon-subtracted magnetic scattering and simulated 2D color plots of neutron scattering data at 5 K with $E_i = 38$ meV, respectively. We presume that the high- $|\mathbf{Q}|$ intensity is mostly phononic in origin and calculated the vibrational part of the scattering at 5 K using the data recorded at 300 K (which is well above the long-range magnetic ordering temperature) after proper normalization with the Bose population factor [36,37],

$$\mathcal{B}(\hbar\omega) = \frac{1}{1 - \exp(-\hbar\omega/k_B T)}. \quad (2)$$

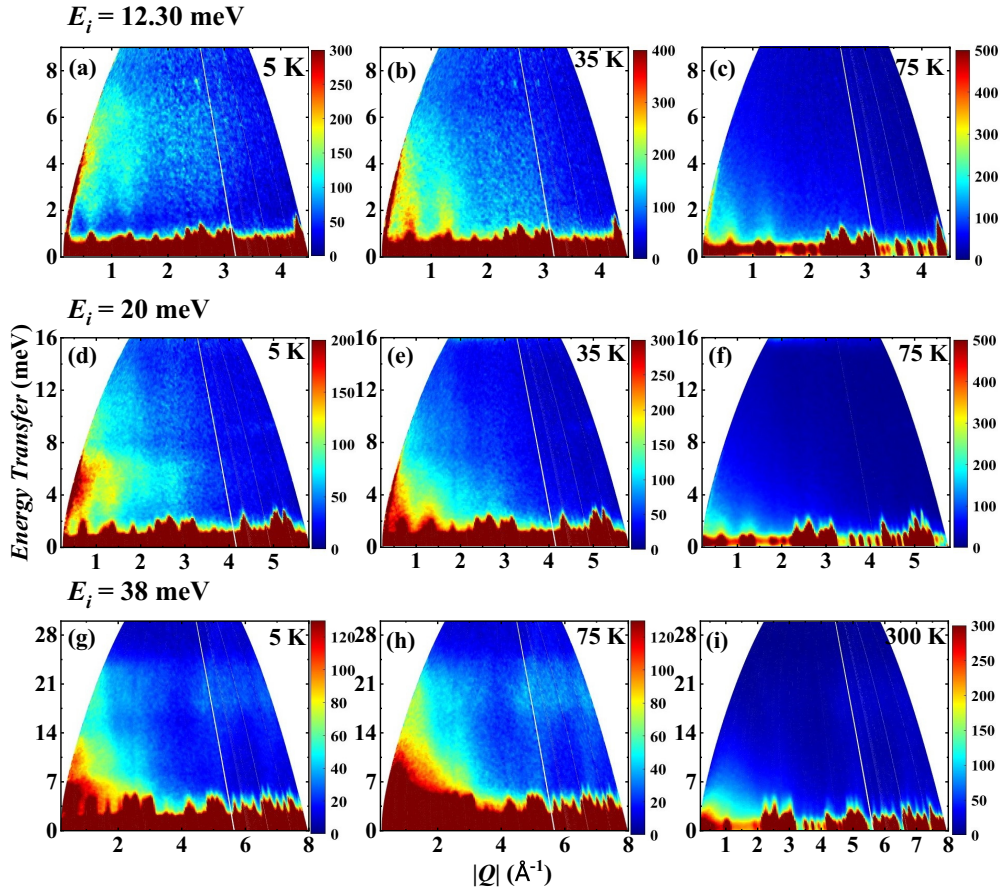


FIG. 4. Two-dimensional (2D) color plot of the inelastic neutron scattering intensity of $\text{CaMn}_7\text{O}_{12}$ as functions of energy transfer ($\hbar\omega$) and momentum transfer ($|\mathbf{Q}|$), measured with incident neutron energy of (a)–(c) $E_i = 12.30$ meV, (d)–(f) 20 meV, and (g)–(i) 38 meV at different temperatures. The color scales show the scattering intensity in an arbitrary unit.

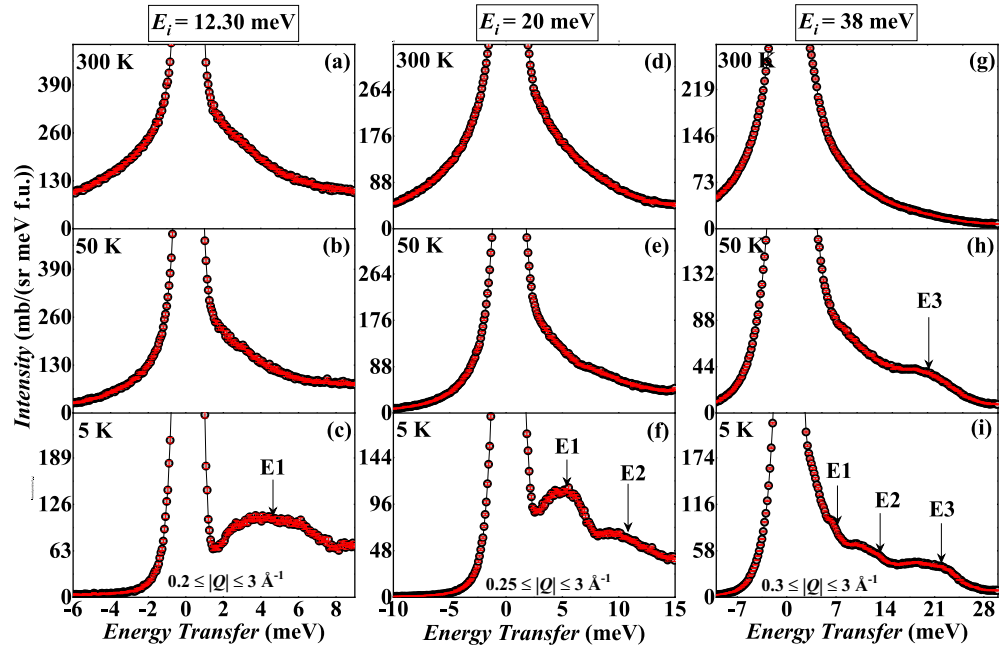


FIG. 5. Scattering intensity as a function of energy transfer for the incident energies $E_i = 12.30$, 20 , and 38 meV. The plots show the data recorded at 5 , 50 , and 300 K. The data at (a)–(c) 12.30 meV, (d)–(f) 20 meV, and (g)–(i) 38 meV are summed over the window of momentum transfer in the range 0.2 – 3.0 \AA^{-1} , 0.25 – 3.0 \AA^{-1} , and 0.3 – 3.0 \AA^{-1} , respectively.

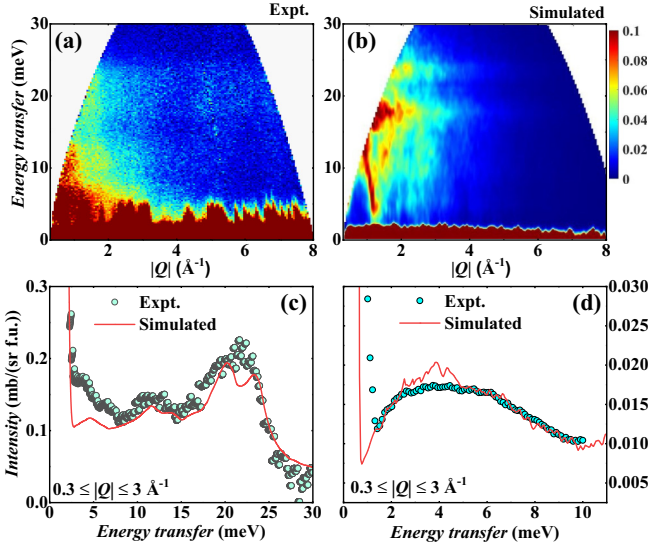


FIG. 6. (a), (b) A comparison of the experimental (phonon-corrected) and the simulated 2D color plot for the incident energy of $E_i = 38$ meV at 5 K. (c) Comparison of the scattering intensity of the experimental and the simulated data as a function of energy transfer with $E_i = 38$ meV over the window of momentum transfer $0.3\text{--}3.0 \text{ \AA}^{-1}$. (d) Similar plots for the incident energy of $E_i = 12.3$ meV.

The Bose corrected 2D color plot is obtained after subtracting the vibrational part from the measured data at 5 K.

The simulated integrated intensity versus energy plots (red continuous line) are shown in Figs. 6(c) and 6(d) for $E_i = 38$ and 12.3 meV, respectively, along with the estimated magnetic scattering intensity (data points). An acceptable agreement is obtained between the experimentally measured and the model-calculated patterns.

It is to be noted that we need to decrease the value of the strongest AFM interaction between Mn1-Mn1 (J_2) by 5% and the FM interaction between Mn1-Mn3 (J_3) by 30% compared to the initial values taken from the DFT calculation for the reproduction of the two lower-energy bands E_1 and E_2 in the simulation. Additionally, the decrease of FM interactions J_4 (between Mn2 and Mn3) and J_5 (between Mn2 and Mn2) by 25% and 32%, respectively, reproduce E_3 close to the experimental data (see Table I). Nevertheless, the signs of different J_i 's remain the same as that of the DFT result [8].

It is now pertinent to know the origin of these three magnetic excitations, E_1 , E_2 , and E_3 . For that purpose, we have plotted the simulated data with a single J_i at a time. The values of J_i 's are chosen from our SpinW simulation (second row of Table I).

(1) First we set all the exchange interaction terms to zero except J_1 , and we observe, more or less, all three excitations E_1 , E_2 , and E_3 . As evident from Fig. 7(a), there are two strong contributions centered at 7 and 16 meV (approximately midpoints of E_1 and E_2). However, the peak around 23 meV (midpoint of E_3) is rather weak. This suggests that J_1 significantly contributes to the magnetic excitations below T_{N2} . J_1 is the nearest-neighbor interaction between Mn1 and Mn2, and the magnetic state below T_{N2} arises primarily from J_1 .

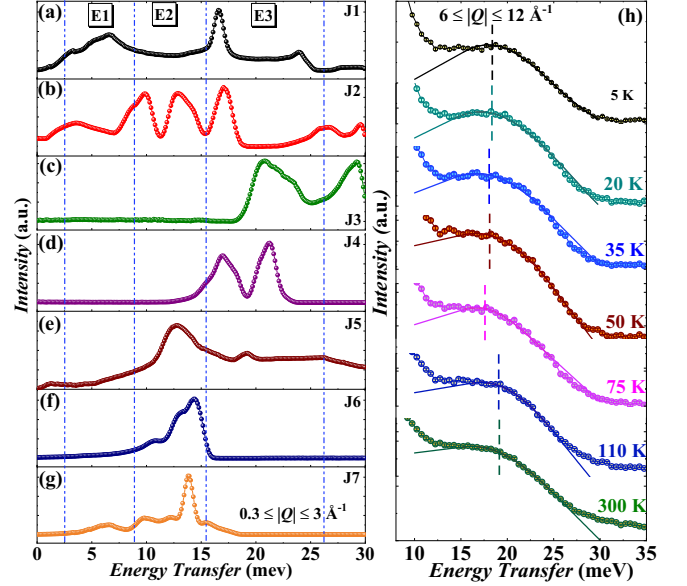


FIG. 7. (a)–(g) Simulated scattering intensity as a function of energy transfer for $E_i = 38$ meV over the window of momentum transfer $0.3\text{--}3.0 \text{ \AA}^{-1}$. Instead of considering seven J_i ($i = 1\text{--}7$) together, the simulation in each panel is performed with only one J_i , and they are represented in different panels. (h) The scattering intensity as a function of energy transfer for the incident energies $E_i = 100$ meV integrated in the high- $|Q|$ range.

(2) Next we have kept J_2 only and set all other interactions to zero. Here we find two broad excitations between 2–19 meV and 25–30 meV [see Fig. 7(b)]. J_2 is the intrachain Mn1-Mn1 interaction and it is the strongest among all J_i 's. Evidently, it contributes to all the excitations.

(3) When we keep J_3 only, there is a broad excitation between 18 and 30 meV [see Fig. 7(c)]; however, no peak is seen below 18 meV. It indicates that J_3 (Mn1-Mn3) possibly has little effect on the magnetic structure below T_{N2} .

(4) When we turn on J_4 with all other $J_i = 0$, clear excitations are seen between 18–22 meV and 22–27 meV, and they may together constitute E_3 observed in our experimental data. Similar to J_3 , J_4 does not contribute towards E_1 and E_2 .

(5) Similarly, we find that J_5 reproduces peak between 12 and 17 meV, which can be identified as E_2 . J_5 is the excitation between nearest-neighbor Mn2-Mn2.

(6) When we turn on J_6 and J_7 (both Mn1-Mn2 next-nearest neighbor) individually, excitations below 18 meV are observed. This indicates that J_6 and J_7 have no role towards the magnetic state $T_{N2} \leq T \leq T_{N1}$. It is to be noted that J_6 is FM, while J_7 is AFM due to a small difference in the Mn1-O-Mn2 bond angle.

3. Magnon-phonon coupling

So far, we have only discussed the low- $|Q|$ part of the excitation spectra. If we carefully look at the high- $|Q|$ part of the $E_i = 38$ meV 2D color plot, a clear band of excitation is seen around 20 meV [see Figs. 4(g) and 4(h)]. The intensity of the band increases with increasing temperature. Clearly, such high- $|Q|$ anomaly is associated with the magnetic excitation observed at the same energy range in the low- $|Q|$ part, and it

indicates the existence of possible magnon-phonon coupling in the system.

Earlier Raman [38] and infrared [35] spectroscopy studies indicated the presence of spin-phonon coupling in CMO. Previous INS data [35] as well as our present INS study (see Fig. 4) also show high- $|\mathbf{Q}|$ intensity at the same energy (around 20 meV) where the magnetic excitation is observed at the low- $|\mathbf{Q}|$ regime. In Fig. 7(h), we have made cuts for the high value of $|\mathbf{Q}|$ and it is shown for different temperatures. A clear peak is observed around E_3 (~ 20 meV), even at high $|\mathbf{Q}|$. We have fitted all the peaks with a Gaussian function (solid lines) to identify the correct peak position. Interestingly, the peak position shifts to lower energy below about T_{N1} , indicating the role of the magnon, which develops in the magnetically ordered phase. A notable decrease in the peak position occurs when the temperature drops from 110 to 75 K. Interestingly, the peak shifts to a slightly higher position at 50 K and then remains nearly constant with further decrease in temperature. A similar shift in the high- $|\mathbf{Q}|$ peak position was observed in other systems showing magnon-phonon coupling [39]. It is to be noted that the peak around 20 meV continues to exist at high $|\mathbf{Q}|$ even above T_{N1} , which can be attributed to paramagnons along with the phonon scattering [35].

IV. DISCUSSION

The previous works on CMO have assigned it to be a mixed-valent compound with 6:1 ratio of Mn^{3+} and Mn^{4+} . The Mn^{4+} ions seem to play an important role in the multiferroicity. Our XANES data in the x-ray absorption study clearly indicate that the compound is indeed mixed valent with the presence of both Mn^{3+} and Mn^{4+} ions. The XANES rising line resides closer to that of the standard Mn_2O_3 than the MnO_2 , which indicates that the majority of Mn is in the 3+ state in CMO.

An important observation of the present work is the structural distortion observed around the magnetic transition temperatures. In the previous works, the overall crystal structure of [14] $\text{CaMn}_7\text{O}_{12}$ was extensively investigated, and a modulated crystal structure below 240 K was found. Our analysis, on the other hand, focuses on the local distortion of the Mn-O polyhedra. We do not find any change in the crystal symmetry and the modulation vector at T_{N1} or T_{N2} ; however, lattice parameters and Mn-O bond lengths show anomalies around the magnetic transition temperatures. Both MnIO_4 square planar and Mn_2O_6 octahedra show considerable distortion with temperature, while the Mn_3O_6 octahedra containing an Mn^{4+} ion at the center remain almost undistorted. In the uniform octahedral coordination, Mn^{4+} ions tend to have stable nondegenerate electronic configurations and are less likely to undergo Jahn-Teller distortion. Lim *et al.* [20] also found negligible displacement of the Mn3 ion from the DFT calculation, which matches well with our data. This justifies that the displacement of the Mn3 charge center has no role in the observed polarization in the system. Notably, the negligible displacement of Mn3 is on par with the DFT+ U + J result of Lim *et al.* [20].

Nevertheless, our PXRD data indicate significant distortion of the MnIO_4 square planar and Mn_2O_6 octahedra at the magnetic transition temperatures. These distortions, which

are generally caused by exchange striction or exchange-driven magnetostriction, occur due to the displacement of the magnetic atoms below the magnetic ordering temperature in order to minimize the total energy of the whole system. Lu *et al.* [8] argued that the ferroelectric polarization is caused by the exchange striction between Mn3 and Mn1 or Mn2 ions. Although Mn3 does not show any positional rearrangement or modulation below T_{N1} , the Mn1-Mn3 and Mn2-Mn3 exchange striction can be operative due to the displacement of the Mn1 and Mn2 ions, respectively. The first-principles-based calculation by Zhang *et al.* [9] indicates noncollinear-type exchange striction in the Mn2-Mn3 chain of the crystal structure, along with the presence of the $p-d$ hybridization mechanism. The DFT + U + J + spin-orbit-coupling (SOC)-based calculation by Lim *et al.* [20] demonstrates that the effect of the exchange striction plays an important role towards the Mn3-O charge distribution. Such models are on par with the observed exchange striction in our structural studies.

As already mentioned, the $E_3 \sim 20$ meV excitation in our INS data is connected to the transition occurring at T_{N1} , and the polarization also develops just at T_{N1} . Therefore, the observed \mathbf{P} is closely connected to the E_3 excitation. In our SpinW calculation with individual J_i [see Figs. 7(a)–7(g)], the major contribution towards E_3 arises from the exchange terms J_3 and J_4 , which actually denote the Mn1-Mn3 and the Mn2-Mn3 interaction terms, respectively. Theoretical calculations [8,9,20] already indicate that the exchange striction in the Mn1-Mn3 and Mn2-Mn3 (particularly the latter one, J_4) plays an important role towards the multiferroicity. Therefore, our simulation in tandem with the PXRD analysis is consistent with the previous conjectures and supports the picture of exchange-striction-induced multiferroicity in the system. It is to be noted that the exchange parameters (such as J_1 , J_2 , J_5 , etc.) associated with the excitations observed below T_{N2} are primarily between Mn1-Mn2, Mn1-Mn1, Mn2-Mn2, and Mn3-Mn3, and have little role towards the polarization as \mathbf{P} does not show any anomaly at T_{N2} . Although our PXRD and XAS work indicate exchange striction both at T_{N1} and T_{N2} , it does not play any role towards the observed polarization at T_{N2} .

The exchange striction is also supported by the change in the pre-edge area of the Mn-K XAS. It is well known that magnetostructural coupling plays an important role in exchange striction. From our high- $|\mathbf{Q}|$ INS data [see Fig. 7(h)], we find the signature of spin-phonon coupling, where the excitation peak shifts to lower energy below about T_{N1} .

In conclusion, we observe a clear signature of exchange striction in our PXRD data in the multiferroic $\text{CaMn}_7\text{O}_{12}$, and our SpinW simulation indicates an important role of Mn1-Mn3 and Mn2-Mn3 exchange terms, which are associated with the transition at T_{N1} , and it possibly plays a pivotal role in the development of concomitant electrical polarization.

ACKNOWLEDGMENTS

J.S. acknowledges SERB-DST, India for the Ramanujan Fellowship [Grant No. RJF/2019/000046(SQUID-1986-JS-3632)]. M.N. would like to thank CSIR, India for his research fellowship [File No. 09/080(1131)/2019-EMR-I]. The

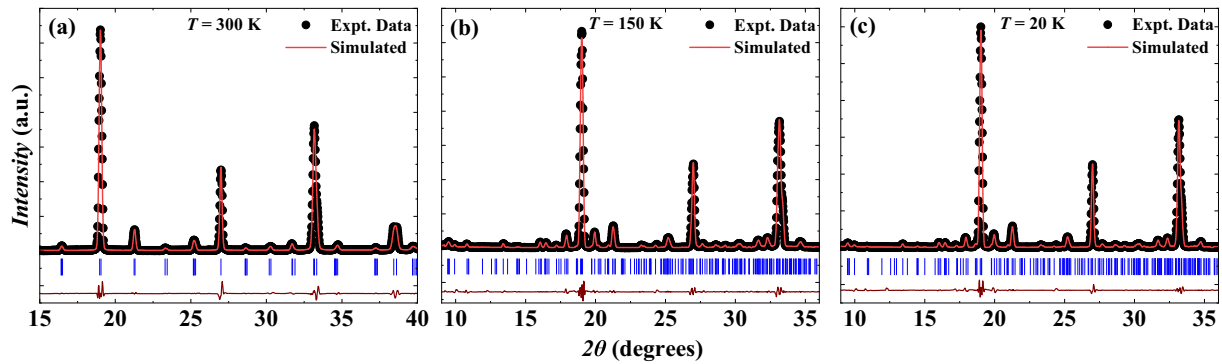


FIG. 8. Rietveld refinement of the synchrotron radiation-based powder diffraction pattern of $\text{CaMn}_7\text{O}_{12}$ recorded at (a) 300 K, (b) 150 K, and (c) 20 K. The solid points represent the measured data, while the solid lines represent the calculated diffraction pattern. The ticks indicate the positions for the Bragg peaks due to the crystal structure of $\text{CaMn}_7\text{O}_{12}$.

Department of Science and Technology (India) is acknowledged for financial support, and Saha Institute of Nuclear Physics and Jawaharlal Nehru Centre for Advanced Scientific Research, India, for facilitating the experiments at the Indian Beam Line, Photon Factory, KEK, Japan. We are thankful for the India-RAL collaborative project (Project No. SR/NM/Z-07/2015) for the neutron scattering studies at the ISIS facility, RAL, UK (Grant No. RB1768021 [26]). The Diamond Light Source (UK) is acknowledged for time

on beam line B-18 under Proposal No. SP17752-1. D.T.A. would like to thank EPSRC UK for the funding (Grant No. EP/W00562X/1).

APPENDIX: REFINEMENT OF PXRD DATA

Figure 8 presents the Rietveld refinement of the PXRD data.

- [1] T. Kimura, T. Goto, H. Shintani, T. A. K. Ishizaka, and Y. Tokura, *Nature (London)* **426**, 55 (2003).
- [2] S.-W. Cheong and M. Mostovoy, *Nat. Mater.* **6**, 13 (2007).
- [3] N. Hur, S. Park, P. A. Sharma, S. Guha, and S.-W. Cheong, *Phys. Rev. Lett.* **93**, 107207 (2004).
- [4] N. Hur, S. Park, P. A. Sharma, J. S. Ahn, S. Guha, and S.-W. Cheong, *Nature (London)* **429**, 392 (2004).
- [5] M. Fiebig, *J. Phys. D: Appl. Phys.* **38**, R123 (2005).
- [6] P. Curie, *J. Phys. Theor. Appl.* **3**, 393 (1894).
- [7] T. Goto, T. Kimura, G. Lawes, A. P. Ramirez, and Y. Tokura, *Phys. Rev. Lett.* **92**, 257201 (2004).
- [8] X. Z. Lu, M. H. Whangbo, S. Dong, X. G. Gong, and H. J. Xiang, *Phys. Rev. Lett.* **108**, 187204 (2012).
- [9] G. Zhang, S. Dong, Z. Yan, Y. Guo, Q. Zhang, S. Yunoki, E. Dagotto, and J.-M. Liu, *Phys. Rev. B* **84**, 174413 (2011).
- [10] R. D. Johnson, L. C. Chapon, D. D. Khalyavin, P. Manuel, P. G. Radaelli, and C. Martin, *Phys. Rev. Lett.* **108**, 067201 (2012).
- [11] J. Sannigrahi, S. Chattopadhyay, D. Dutta, S. Giri, and S. Majumdar, *J. Phys.: Condens. Matter* **25**, 246001 (2013).
- [12] M. Nakamura, Y. Tokunaga, M. Kawasaki, and Y. Tokura, *Appl. Phys. Lett.* **98**, 082902 (2011).
- [13] J. Sannigrahi, S. Bhowal, S. Giri, S. Majumdar, and I. Dasgupta, *Phys. Rev. B* **91**, 220407(R) (2015).
- [14] W. Sławiński, R. Przeniosło, I. Sosnowska, M. Bieringer, I. Margiolaki, and E. Suard, *Acta Cryst. B* **65**, 535 (2009).
- [15] R. D. Johnson, D. D. Khalyavin, P. Manuel, A. Bombardi, C. Martin, L. C. Chapon, and P. G. Radaelli, *Phys. Rev. B* **93**, 180403(R) (2016).
- [16] N. J. Perks, R. D. Johnson, C. Martin, L. C. Chapon, and P. G. Radaelli, *Nat. Commun.* **3**, 1277 (2012).
- [17] K. Cao, R. D. Johnson, N. Perks, F. Giustino, and P. G. Radaelli, *Phys. Rev. B* **91**, 064422 (2015).
- [18] J.-Q. Dai, Y.-M. Song, and H. Zhang, *New J. Phys.* **17**, 113038 (2015).
- [19] J. T. Zhang, X. M. Lu, J. Zhou, H. Sun, F. Z. Huang, and J. S. Zhu, *Phys. Rev. B* **87**, 075127 (2013).
- [20] J. S. Lim, D. Saldana-Greco, and A. M. Rappe, *Phys. Rev. B* **97**, 045115 (2018).
- [21] V. Petříček, M. Dušek, and L. Palatinus, *Z. Kristallogr.* **229**, 345 (2014).
- [22] V. Petříček, L. Palatinus, J. Plášil, and M. Dušek, *Z. Kristallogr.* **238**, 271 (2023).
- [23] M. Newville, *J. Synchrotron Radiat.* **8**, 322 (2001).
- [24] B. Ravel and M. Newville, *J. Synchrotron Radiat.* **12**, 537 (2005).
- [25] R. I. Bewley, R. S. Eccleston, K. A. McEwen, S. M. Hayden, M. T. Dove, S. M. Bennington, J. R. Treadgold, and R. L. S. Coleman, *Phys. B: Condens. Matter* **385-386**, 1029 (2006).
- [26] S. Majumdar, J. Sannigrahi, and D. Adroja, *ISIS Facility*, 1768021 (2017).
- [27] M. Nakamura, R. Kajimoto, Y. Inamura, F. Mizuno, M. Fujita, T. Yokoo, and M. Arai, *J. Phys. Soc. Jpn.* **78**, 093002 (2009).
- [28] M. Russina and F. Mezei, *Nucl. Instrum. Methods Phys. Res. Sect. A* **604**, 624 (2009).
- [29] O. Arnold *et al.*, *Nucl. Instrum. Methods Phys. Res. Sect. A* **764**, 156 (2014).
- [30] S. Toth and B. Lake, *J. Phys.: Condens. Matter* **27**, 166002 (2015).

- [31] F. Bridges, C. H. Booth, M. Anderson, G. H. Kwei, J. J. Neumeier, J. Snyder, J. Mitchell, J. S. Gardner, and E. Brosha, *Phys. Rev. B* **63**, 214405 (2001).
- [32] F. Bridges, C. H. Booth, G. H. Kwei, J. J. Neumeier, and G. A. Sawatzky, *Phys. Rev. B* **61**, R9237 (2000).
- [33] B. Poumellec, V. Kraizman, Y. Aifa, R. Cortès, A. Novakovich, and R. Vedrinskii, *Phys. Rev. B* **58**, 6133 (1998).
- [34] O. Šipr, A. Šimůnek, S. Bocharov, T. Kirchner, and G. Dräger, *Phys. Rev. B* **60**, 14115 (1999).
- [35] F. Kadlec, V. Goian, C. Kadlec, M. Kempa, P. c. v. Vaněk, J. Taylor, S. Rols, J. Prokleška, M. Orlita, and S. Kamba, *Phys. Rev. B* **90**, 054307 (2014).
- [36] S.-H. Do, S.-Y. Park, J. Yoshitake, J. Nasu, Y. Motome, Y. S. Kwon, D. T. Adroja, D. J. Voneshen, K. Kim, T.-H. Jang, J.-H. Park, K.-Y. Choi, and S. Ji, *Nat. Phys.* **13**, 1079 (2017).
- [37] H. S. Nair, M. O. Ogunbunmi, C. M. N. Kumar, D. T. Adroja, P. Manuel, D. Fortes, J. Taylor, and A. M. Strydom, *J. Phys.: Condens. Matter* **29**, 345801 (2017).
- [38] A. Nonato, B. S. Araujo, A. P. Ayala, A. P. Maciel, S. Yanez-Vilar, M. Sanchez-Andujar, M. A. Senaris-Rodriguez, and C. W. A. Paschoal, *Appl. Phys. Lett.* **105**, 222902 (2014).
- [39] X. Chen, D. Bansal, S. Sullivan, D. L. Abernathy, A. A. Aczel, J. Zhou, O. Delaire, and L. Shi, *Phys. Rev. B* **94**, 134309 (2016).